

Measuring Deformation in the Mouse Optic Nerve Head and Peripapillary Sclera

Cathy Nguyen,¹ Dan Midgett,² Elizabeth C. Kimball,¹ Matthew R. Steinhart,¹ Thao D. Nguyen,^{2,3} Mary E. Pease,¹ Ericka N. Oglesby,¹ Joan L. Jefferys,¹ and Harry A. Quigley¹

¹The Glaucoma Center of Excellence, Wilmer Ophthalmological Institute, Baltimore, Maryland, United States

²Department of Mechanical Engineering, Johns Hopkins University, Baltimore, Maryland, United States

³Department of Materials Science, Johns Hopkins University, Baltimore, Maryland, United States

Correspondence: Harry A. Quigley, Wilmer Eye Institute 122, Johns Hopkins Hospital, Baltimore, MD 21287, USA; hquigley@jhmi.edu.

Submitted: August 26, 2016
Accepted: December 12, 2016

Citation: Nguyen C, Midgett D, Kimball EC, et al. Measuring deformation in the mouse optic nerve head and peripapillary sclera. *Invest Ophthalmol Vis Sci.* 2017;58:721–733. DOI: 10.1167/iov.16-20620

PURPOSE. To develop an ex vivo explant system using multiphoton microscopy and digital volume correlation to measure the full-field deformation response to intraocular pressure (IOP) change in the peripapillary sclera (PPS) and in the optic nerve head (ONH) astrocytic structure.

METHODS. Green fluorescent protein (GFP)-glutamate transporter-GLT1 (GLT1/GFP) mouse eyes were explanted and imaged with a laser-scanning microscope under controlled inflation. Images were analyzed for regional strains and changes in astrocytic lamina and PPS shape. Astrocyte volume fraction in seven control GLT1/GFP mice was measured. The level of fluorescence of GFP fluorescent astrocytes was compared with glial fibrillary acidic protein (GFAP) labeled astrocytes using immunohistochemistry.

RESULTS. The ONH astrocytic structure remained stable during 3 hours in explants. Control strain—globally, in the central one-half or two-thirds of the astrocytic lamina—was significantly greater in the nasal-temporal direction than in the inferior-superior or anterior-posterior directions (each $P \leq 0.03$, mixed models). The PPS opening (perimeter) in normal eye explants also became wider nasal-temporally than superior-inferiorly during inflation from 10 to 30 mm Hg ($P = 0.0005$). After 1 to 3 days of chronic IOP elevation, PPS area was larger than in control eyes ($P = 0.035$), perimeter elongation was 37% less than controls, and global nasal-temporal strain was significantly less than controls ($P = 0.007$). Astrocyte orientation was altered by chronic IOP elevation, with processes redirected toward the longitudinal axis of the optic nerve.

CONCLUSIONS. The explant inflation test measures the strain response of the mouse ONH to applied IOP. Initial studies indicate regional differences in response to both acute and chronic IOP elevation within the ONH region.

Keywords: glaucoma, sclera, optic nerve head, mouse, retinal ganglion cell, extracellular matrix, collagen

The development and severity of glaucoma damage to retinal ganglion cell (RGC) axons are associated with exposure to the intraocular pressure (IOP), including the mean level,¹ fluctuation,² and peak level of IOP.³ Intraocular pressure deforms the optic nerve head (ONH) through the following two boundary conditions: (1) the translaminar pressure gradient between the intraocular and the orbital optic nerve tissues across the ONH and (2) the tensile stresses generated in the walls of the peripapillary sclera (PPS) that are transmitted to ONH tissues.^{4–8} The deformation of the neural and connective tissues of the ONH arising from the interaction of these two loading conditions depends on the mechanical properties of the PPS and the ONH tissue structure supporting RGC axons as they leave the intraocular space. Optic nerve head deformation in glaucoma is associated with interruption of anterograde and retrograde RGC axonal transport, leading to axon degeneration and RGC somal death by apoptosis^{9,10} in human glaucoma and in experimental monkey and rodent glaucoma models. Experiments in human and monkey eyes have shown that the initial location of RGC axon damage occurs where the relative

density of connective tissues in the ONH is lower.^{11,12,13} Regions with lower connective tissue volume fraction may be more mechanically compliant and incur larger IOP-generated deformation.¹⁴ Variations in PPS and ONH mechanical properties likely contribute to the fact that half of those with open angle glaucoma suffer injury in the normal IOP range.¹⁵

Scleral biomechanics have been studied by ex vivo inflation testing with two-dimensional (2D) and three-dimensional (3D) surface deformation mapping of human,¹⁶ monkey,¹⁷ and mouse¹⁸ eyes subjected to experimental glaucoma. These studies have found that the sclera is stiffer (exhibiting less strain) in older eyes and in diagnosed glaucoma eyes. In glaucoma human eyes, the effect is localized and anisotropic, with smaller strains along some scleral meridians than others. Previous investigations of posterior ocular mechanical behavior have been limited to the sclera because of the relative inaccessibility and complex structure of the ONH. It is the unique interaction between the PPS and the ONH that may determine IOP-induced effects on RGC axons.⁷ A better understanding of the biomechanics of the ONH and PPS,

individually and together, may improve predictions of the development and progression of glaucomatous axonal damage, leading to new therapeutic approaches.¹⁹

Mouse models can be used to elucidate the conjoined mechanical responses of the PPS and ONH. The morphology and spatial arrangement of the cellular processes of the astrocytes are similar to those of the collagen beams in the human lamina cribrosa.²⁰ Rodent eyes that are subjected to experimental increases in IOP have neuronal, glial, and associated tissue alterations in RGCs that are phenotypically similar to human glaucoma.^{21,22,23} Similar to the human eye,²⁴ the mouse PPS has circumferentially arranged collagen and elastin fibers, and in both species this anisotropy is disrupted by glaucoma.²⁵ In both human and mouse eyes, glaucoma injures RGC axons at the ONH and only RGC die with the preservation of other retinal neurons.^{26,27}

Some have questioned whether the cellular lamina of the mouse or rat is load-bearing in a similar manner and magnitude to that of monkey and human eyes. We previously developed an *ex vivo* inflation test that used 2D digital image correlation to study the deformation of the mouse sclera under controlled pressurization. The pressure-strain behavior of the sclera demonstrated a stiffer and less anisotropic response after chronic IOP elevation.²⁸ Here, we report for the first time the study of both PPS and ONH in freshly excised mouse eyes under controlled inflation using laser-scanning multiphoton microscopy and digital volume correlation (DVC) for 3D deformation mapping of the image volume. Digital volume correlation has been applied previously by Girard et al.²⁹ to analyze *in vivo* optical coherence tomography (OCT) scans of the human PPS and lamina cribrosa after IOP-lowering surgery. Digital volume correlation was also used by Coudrillier et al.³⁰ to analyze phase contrast micro-computed tomography imaging of the pig lamina. The present study presents the first full-field measurements of the pressure-induced deformation of the mouse ONH tissues with acute IOP elevation in both normal mouse eyes and mouse eyes subjected to chronic IOP elevation for short periods. This *ex vivo* explant system allows for detailed analysis of IOP-induced strain and provides a platform to test treatments that can beneficially modulate the scleral response to IOP.

METHODS

Animals

The experiments used 4- to 6-month-old green fluorescent protein (GFP)-glutamate transporter-GLT1 mice (GLT1/GFP; acquired from Jeffrey Rothstein, Johns Hopkins School of Medicine),³¹ which co-express GFP with the glutamate transporter protein, GLT1.³² All animals and experiments were conducted in accordance with guidelines set forth by the ARVO Statement for the Use of Animals in Ophthalmic and Vision Research using protocols approved and monitored by the Johns Hopkins University School of Medicine Animal Care and Use Committee (Baltimore, MD, USA).

Chronic IOP Elevation Model

Mice were anesthetized with a mixture of ketamine (Fort Dodge Animal Health, Fort Dodge, IA, USA), xylazine (VedCo, Inc., Saint Joseph, MO, USA), and acepromazine (Phoenix Pharmaceuticals, Burlingame, CA, USA; 50, 10, and 2 mg/kg, respectively). One anterior chamber was injected with Polybead Microspheres (Polysciences, Inc., Warrington, PA, USA), consisting of 2 μ L of 6- μ m diameter beads and then 2 μ L of 1- μ m diameter beads followed by 1 μ L of viscoelastic compound

(10 mg/mL sodium hyaluronate, Healon; Advanced Medical Optics, Inc., Santa Ana, CA, USA). The injections were made through a 50- μ m diameter tip glass cannula connected to a Hamilton syringe (Hamilton, Inc., Reno, NV, USA). We measured IOP with the Tonolab tonometer (TioLat, Inc., Helsinki, Finland) under anesthesia by inhalation of isoflurane using the RC2-Rodent Circuit Controller (VetEquip, Inc., Pleasanton, CA, USA).

Explant Preparation

Mouse eyes were rapidly enucleated, the optic nerve removed with a razor blade behind the PPS, and the unfixed eye was glued at the cornea to a plastic fixture (Fig. 1). The anterior chamber was cannulated with a 30-gauge needle to set the IOP, which was controlled using a water column. The specimen and plastic holder were mounted onto a platform with tilt-correcting gears for rotation about two axes (Fig. 1A). The platform was situated on the stage of a Zeiss laser-scanning microscope (LSM 710 NLO; Carl-Zeiss, Oberkochen, Germany). The tilt correcting gears were adjusted to align the posterior surface of the ONH perpendicular to the imaging objective. The eye was immersed in PBS to avoid dehydration.

Imaging

A Zeiss laser-scanning microscope with a Chameleon Ultra II laser was used to acquire sequential images of the two-photon fluorescence (TPF) signal of the astrocytic lamina and the second harmonic generation (SHG) signal of the PPS. The TPF images of the astrocytes and SHG images of the collagen were acquired separately because they require different excitation wavelengths. For TPF, which occurs when a fluorophore is excited by the simultaneous absorption of two photons, the laser was tuned to 895 nm and a 500- to 550-nm band pass filter was used to collect the backscattered TPF signal through the 20 \times W Plan Apochromat objective. Images were collected at 1024 \times 1024 pixel resolution, with a pixel conversion factor of 1 pixel = 0.415 μ m. The baseline IOP was set to 10 mm Hg and subsequent IOPs to 15, 20, and 30 mm Hg. The specimen was equilibrated for 1 minute after each pressure increase to reduce the effects of creep on the DVC displacement error, as discussed in the following section.

An increase in IOP from the baseline 10 mm Hg led to substantial posterior translation of the astrocytic lamina caused by the inflation of the sclera. To capture this large displacement, we would need to scan a large distance in Z, and the longer imaging time would result in more creep during image acquisition and larger errors in the DVC displacement correlation. We accounted for this translation by identifying a distinct landmark in the astrocytic lamina at the baseline pressure before imaging. After the pressure was increased, the starting Z-position of the scan was adjusted to relocate the feature and position it within the Z-stack at the same location as in the baseline IOP. The resulting Z-motion in μ m was recorded from the micrometer scale of the laser scanning microscope. This Z-motion was then added back to the DVC posterior displacement as a rigid-body motion in Z, and does not affect the strain calculation in the lamina. Using this protocol, each Z-stack was acquired in approximately 2 minutes and covered 75 to 100 μ m of depth, with image slices spaced every 1 μ m.

To image the collagenous PPS, the IOP was lowered back to 10 mm Hg and again raised to 15, 20, and 30 mm Hg for SHG imaging. The specimen was equilibrated for 1 minute at each pressure. Second harmonic generation is a nonlinear optical process where two photons are absorbed and converted into a single photon at twice the excitation energy emitted coher-

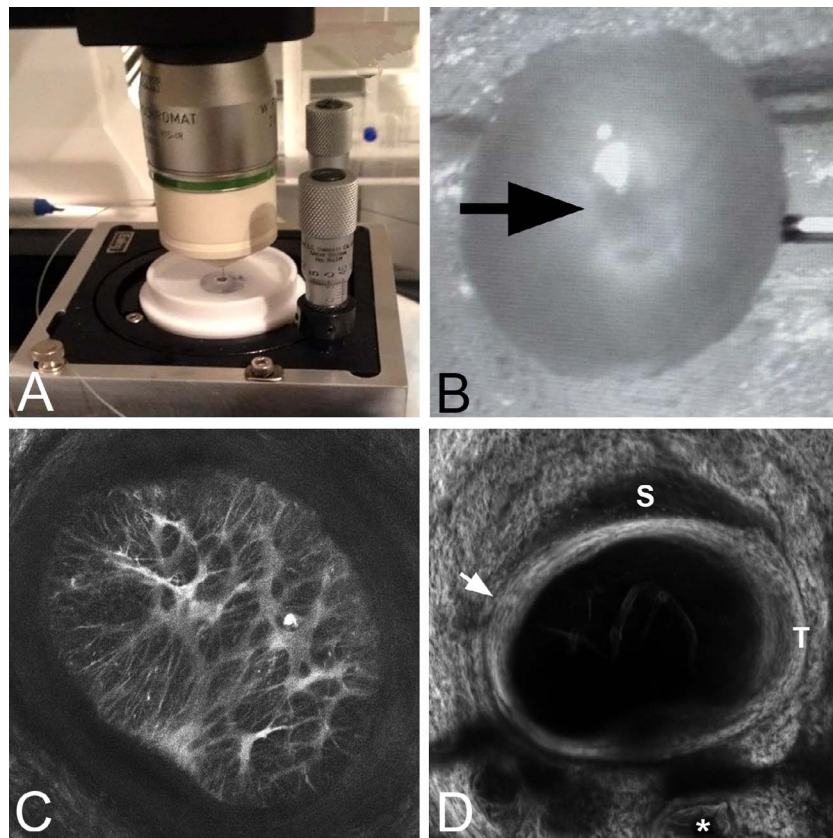


FIGURE 1. (A) The inflation test chamber for mouse eyes with two tilt-correcting gears mounted on the imaging stage. (B) Optic nerve head area (*arrow*) facing the objective lens with the globe cannulated. (C) The maximum-intensity projection of a Z-stack from imaging the astrocytes in the ONH and surrounding sclera (see Supplementary Movie S3 for a video in color through the Z-stack) at 10 mm Hg. (D) Second harmonic generation image of PPS surrounding the ONH at 10 mm Hg. This is a summation of the slices through Z projection image of the PPS. Superior (S) and temporal (T) margins are indicated. The inner scleral contact zone is indicated by the *arrow* and one of three vascular channels passing through the inferior sclera is marked by an *asterisk*.

ently and takes place in systems lacking a center of symmetry. Imaging of the PPS was conducted using an excitation wavelength of 790 nm and collection with a SP470 filter (Chroma Technology Corporation, Bellows Falls, VT, USA).

Effects of Creep

We studied the effect of creep on the Z-displacement of the astrocytic lamina in four specimens. For each specimen, a distinctive landmark was identified at the baseline IOP of 5 mm Hg, and the pressure was increased from 5 to 20 mm Hg, then decreased back to 5 mm Hg in increments of 5 mm Hg. The specimen was equilibrated at each pressure step for 5 minutes, and the Z-motion of the landmark was tracked and recorded every 30 seconds during the course of 5 minutes to measure the creep in lamina position (see Supplementary Fig. S1). The lamina displaced posteriorly with an increase in IOP and anteriorly with a decrease in IOP. In this study, 75% of the displacement occurred during the first 15 seconds after IOP elevation with each IOP change (see Supplementary Table S2). The creep rate was calculated as the slope of the linear regression of the displacement measurements from 15 seconds after elevation to 5 minutes. The creep rate in $\mu\text{m}/\text{min}$ was greater at lower IOP and averaged $1.03 \pm 0.56 \mu\text{m}/\text{min}$. The creep rate decreased with time and was $<1 \mu\text{m}/\text{minute}$ after 1 minute.

Tissue creep during image acquisition has an adverse effect on the positional accuracy of DVC. To minimize this effect, we chose the imaging settings described above to limit the Z-stack

acquisition time to 2 minutes. Furthermore, specimens were allowed to equilibrate for 1 minute before imaging to reduce the creep rate to $<1 \mu\text{m}/\text{minute}$. We evaluated the DVC baseline displacement error, as described later, to confirm that the effect of creep on the DVC accuracy was small. The baseline displacement error consists of both the DVC correlation error for that pressure and the effects of creep. The results of this analysis, presented later, show that for most specimens, the baseline error was <1 pixel in the X, Y, and Z displacement components.

DVC Analysis

For DVC, Z-stacks were reconstructed in a 3D matrix of intensity values in MATLAB (MathWorks, Inc., Natick, MA, USA) with the X and Y direction aligned with the horizontal (nasal-temporal) and vertical (inferior-superior) axes and the Z direction aligned with the anterior-posterior axis. Both SHG and TPF images exhibited significant regional variation in average image intensity. To correct for this and to improve subsequent correlation, the Contrast Limited Adaptive Histogram Equalization algorithm in Fiji Is Just ImageJ (FIJI)³³ was applied to both the SHG and TPF image volumes along with a $3 \times 3 \times 3$ pixel median prefilter to remove pixel-level noise. TPF and SHG images at 10 and 30 mm Hg were analyzed by the Fast Iterative DVC (FIDVC) algorithm developed previously by Bar-Kochba et al.³⁴ to obtain the 3D displacement field in the ONH and PPS volumes. In DVC, the image intensity distribution within subvolumes between a reference volume at 10 mm Hg

and the deformed volume at 30 mm Hg were compared to obtain the displacement field. The FIDVC algorithm determines the displacements by maximizing the cross-correlation of the image intensity of subvolumes in the reference and deformed images.³¹ The algorithm iteratively refines the subvolume size and calculation spacing to improve the correlation in a four-step process starting with a subset size of $128 \times 128 \times 64$ pixels and calculation spacing of $32 \times 32 \times 16$, and ending with a final subset size of $32 \times 32 \times 16$ and spacing of $4 \times 4 \times 1$ pixels. The cross-correlation coefficient provided by the FIDVC algorithm was normalized and exported for analysis along with the components of the calculated displacement field at each point.

Postprocessing DVC Displacements

The DVC displacement fields contained regions of high correlation error that were removed prior to calculating strains. In the TFP images of the astrocytic lamina, this involved removing the PPS portion of the images. For SHG images of the PPS, we removed areas of poor contrast that were indicative of vascular channels (see, e.g., Fig. 1D). These low-contrast areas were identified and removed by setting a lower threshold of 0.03 for the cross-correlation coefficient. We found in preliminary analyses that a lower correlation coefficient threshold of 0.03 removed only dark, featureless areas with poor correlation. A 3D Gaussian filter of width 13 ($21.6 \mu\text{m}$) and standard deviation of 3 ($5 \mu\text{m}$) and a threshold filter (displacements of $< 2 \mu\text{m}$ were removed) were also applied to remove outliers (sharp spikes) in the displacement fields prior to strain calculation. To justify these settings and also to select the optimum DVC correlation subset size, we calculated the DVC displacement and strain errors for a numerically applied strain field (Supplementary Figs. S4-S5). It was found that applying the Gaussian prefilter before calculating strains reduced average strain errors and their standard deviation. Filter sizes of 7 or less had higher errors when compared with filter sizes of 9 or above, and the filter size of 13 had minimum error (Supplementary Fig. S6). This analysis also demonstrated that for subset sizes of 64, 48, 32, and 24, the subset size 32 had the lowest strain errors (Supplementary Fig. S7; see Supplementary Table S8 for numerical displacements and strains with varying filter and subset sizes).

DVC Strain Calculation

The Green-Lagrange strain tensor was evaluated from the DVC displacement field according to Equation 1:

$$[\mathbf{F}] = \begin{bmatrix} 1 + U_{X,X} & U_{X,Y} & U_{X,Z} \\ U_{Y,X} & 1 + U_{Y,Y} & U_{Y,Z} \\ U_{Z,X} & U_{Z,Y} & 1 + U_{Z,Z} \end{bmatrix},$$

$$[\mathbf{E}] = \frac{1}{2}([\mathbf{F}]^T[\mathbf{F}] - [\mathbf{I}]), \quad (1)$$

where \mathbf{I} is the identity tensor. The partial derivatives of the DVC displacement components, U_X , U_Y , and U_Z were calculated by fitting a sixth-order polynomial function across X or Y and a linear function in Z and evaluating the derivative. Preliminary studies that used higher order polynomials to smooth the displacement components did not significantly affect the strain calculations. Using a higher-order fit in Z resulted in large fluctuations in E_{zz} , the normal strain along the thickness direction, caused by increasing displacement correlation error for U_z with depth. This was a result of poorer out-of-plane resolution and the fading of the signal at deeper slices.

We chose a linear fit to calculate the average out-of-plane strain response of the astrocytic lamina.

Error Analysis

To calculate displacement errors, DVC was used to correlate the duplicate Z -stacks acquired at the baseline IOP of 10 mm Hg. Because the two image volumes were acquired consecutively under the same conditions, the displacement fields should ideally be zero. The baseline positional error e_I was evaluated as:

$$e_I = \sqrt{\frac{1}{M} \sum_j^M U_{I,j}^2}, \quad (2)$$

where I denotes the X , Y , or Z direction, M is the total number of material points used in the DVC calculations, and $j = 1 \dots M$. In addition, the bias and uncertainty were defined as the mean and standard deviation of the DVC displacement fields in X , Y , and Z . Baseline error therefore includes the DVC correlation error and tissue creep during image acquisition.

Perimeter Tracing

The perimeter of the astrocytic lamina was marked by importing the contrast enhanced TFP image sets at IOP 10 mm Hg and 30 mm Hg into FIJI and using the manual polygon tool to select points on the ONH boundary between the area of fluorescent astrocytes and the surrounding PPS region. The ONH perimeter was computed by summing the lengths of the line segments connecting the points. Initially, the perimeter was marked in each of 10 individual slices equally spaced through the Z -stack to determine if there was regional change in perimeter through the ONH with IOP elevation. Because the perimeter showed little variation with depth, the remainder of the analysis was carried out using the marked perimeter from the 2D average intensity projection along the Z -axis. This 2D perimeter was used in three different analyses. First, we computed the perimeter elongation as the change in the marked perimeter with change in pressure from 10 to 30 mm Hg for the 2D average intensity projection:

$$\text{perimeter elongation} = \frac{c_t - C_T}{C_T}, \quad (3)$$

where c_t is the marked perimeter at 30 mm Hg and C_T is the marked perimeter at 10 mm Hg. Second, an ellipse was fitted to the points of the marked perimeter at 10 mm Hg and used to define the central and peripheral regions to analyze regional variations in ONH strains. Third, the perimeter tracing was used to determine the area of the ONH and to estimate the percentage of the overall ONH area that exhibited accurate DVC displacement correlation.

ONH DVC Regional Strains

The strains of the astrocytic lamina were calculated for the full ONH, for two-thirds of the central ONH, and for its central and peripheral regions. The regions were determined by fitting an ellipse to the perimeter tracing of the average intensity projection, denoted as the outer elliptical region. The two-thirds of the central ONH was defined by a concentric ellipse of the same shape but with two-thirds of the area of the outer ellipse. The central region was defined by a concentric ellipse of the same shape but with half the area of the outer ellipse (Fig. 2). These regional calculations were performed because we noted that the correlation was not as consistent in the

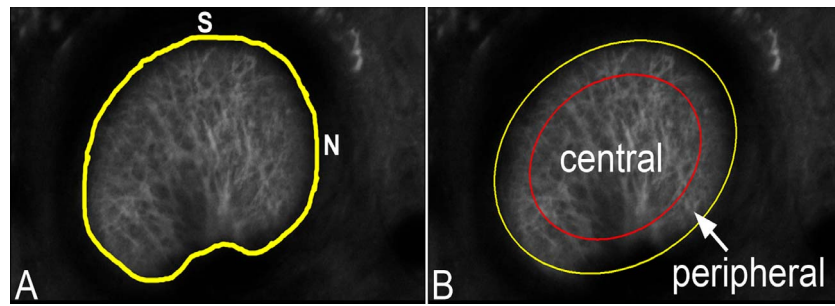


FIGURE 2. (A) Control GLT1/GFP optic nerve area of a 2D Z-averaged intensity projection of the astrocytic lamina with its perimeter delineated in yellow (superior [S] and nasal [N]) at baseline pressure. (B) An ellipse was fitted to the marked perimeter (yellow line) and an inner ellipse (red line) was calculated to include one-half of the optic nerve area.

peripheral lamina. The DVC strains in the nasal-temporal direction (along the X -axis, denoted E_{XX}) and the superior-inferior direction (along the Y -axis, E_{YY}) were averaged over the central volume and peripheral volume.

ONH Area of Correlation

Within the astrocytic lamina, there were areas of each ONH where DVC was unable to correlate between pressures successfully. To indicate the proportion of the ONH that provided useful data for strain calculation, we calculated the percentage of the ONH (within the marked perimeter) for which DVC correlation was defined as accurate using the criterion that the correlation coefficients were greater than 0.03. To determine this percentage, the accurate DVC U_x displacement components in the region of the astrocytic lamina were averaged in the Z direction. A contour plot of the averaged displacement was imported into FIJI (Fig. 3B). The region occupied by the X -averaged displacements was traced, and its area was divided by overall ONH area to determine the percentage of the ONH area that had correlated accurately (Fig. 3).

Astrocyte Volume Fraction

Individual images from the middle of the Z -stack of the astrocytic structure in the ONH were used to calculate astrocyte volume fraction. Images were cropped (removing sclera and other non-ONH material) then converted to grayscale. Using automated Metamorph software (MetaMorph Microscopy Automation & Image Analysis Software, Molecular

Devices, Downingtown, PA, USA), binary images were produced using a thresholding setting, only including pixels within a set grayscale limit defined for each specimen. Then, area and scale factor parameter filters created an overlay representative of the total astrocytic area. These settings were optimized such that the Metamorph representative image matched the original TPF image. The astrocyte volume fraction was defined as the astrocyte area divided by total ONH area.

Histological Study

After biomechanical testing, some PPS and ONH tissues were embedded in an optimal cutting temperature compound and frozen sectioned at $6\text{-}\mu\text{m}$ thickness for immunofluorescent antibody labeling for the astrocytic marker, glial fibrillary acidic protein (GFAP; Abcam, Cambridge, MA, USA). Tissue sections were incubated overnight in primary antibody solution and blocking buffer. Samples were then exposed to goat anti-rabbit Cy3 secondary (1:200; Jackson ImmunoResearch, West Grove, PA, USA). Finally, nuclei were counterstained with 4',6-diamidino-2-phenylindole (DAPI; Invitrogen, Carlsbad, CA, USA). Samples were cover slipped with DAKO mounting media (DAKO, Carpinteria, CA, USA) and imaged with a Zeiss LSM 710 Confocal Microscope (Zeiss MicroImaging, Thornwood, NY, USA) using a $20\times$ lens.

Statistical Testing

For comparisons of normally distributed data, t -tests were used, whereas for data that was not normally distributed, Mann-Whitney U tests were used. For regional comparisons of strain

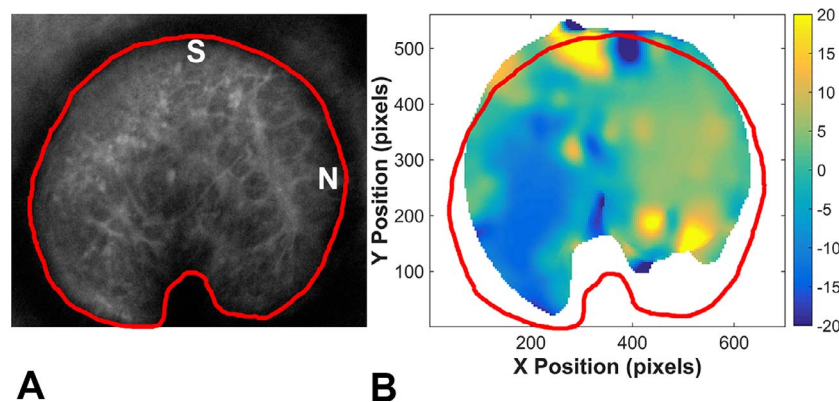


FIGURE 3. (A) A 2D Z-averaged intensity projection of a control GLT1/GFP astrocytic lamina at baseline pressure with the optic nerve area outlined in red and oriented with the superior (S) on top and nasal (N) on the right. (B) For a Z-stack imaged at 10 and 30 mm Hg, the area in which DVC correlation was accurate is shown in the colored area, and the degree/direction of displacement indicated by DVC is shown by the color shading in the contour plot. The ONH area is outlined in red. Note that correlation was least likely in the more peripheral ONH.

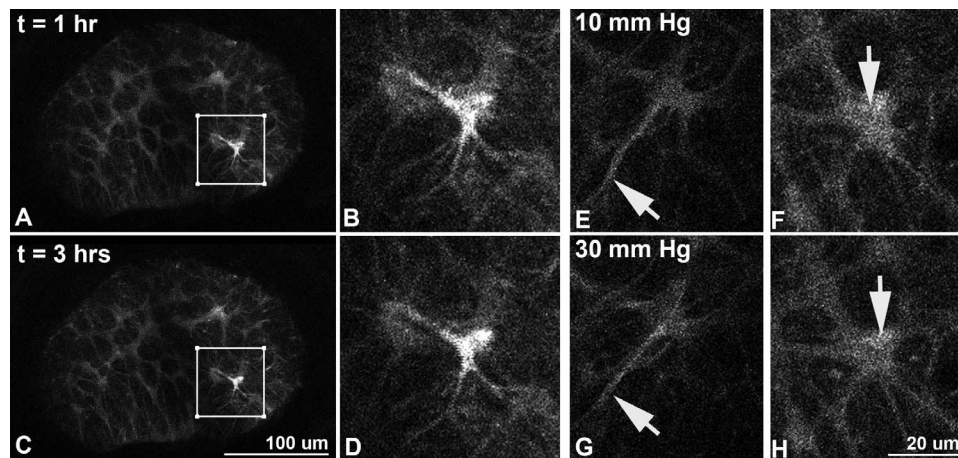


FIGURE 4. Two-photon fluorescence images illustrating the detailed structure of mouse ONH astrocytes remaining stable for 3 hours in control GLT1/GFP explants (A, C = lower magnification; B, D = higher magnification) at 10 mm Hg. When IOP was increased from 10 mm Hg (E, F) to 30 mm Hg (G, H) for 2 hours, visible changes were detected in astrocyte somal shape (F, H: astrocyte soma elongates) and process orientation (E, G: astrocyte process straightens; *arrows*; magnification factor bar indicates 100 μ m in A and C and 20 μ m in B, D-H).

data, all estimates and P values are from mixed models that take into account correlations among repeat measurements on a single eye. Repeat measurements from the three directions (nasal-temporal, inferior-superior, anterior-posterior) or two regions (central, peripheral) were assumed to have an exchangeable correlation structure, in which any two measurements have the same correlation. For all models, least squares means and 95% confidence limits were used to estimate mean strain. For models analyzing the effect of direction, the Tukey-Kramer method was used to adjust pairwise significance levels for multiple comparisons. Statistical analyses were performed using SAS 9.2 (SAS Institute, Cary, NC, USA).

RESULTS

Astrocyte Morphology

To assess possible deterioration in the integrity of cellular structure over time in the explant system, we imaged specimens hourly for 3 hours while maintaining an IOP of 10 mm Hg. Neither the overall structure nor the detailed appearance of individual astrocytes changed discernibly (Figs. 4A-D). When IOP was elevated from 2 hours, astrocytic somal and process structure changed from their baseline appearance at 10 mm Hg (Figs. 4E-H).

Volume Fraction of Astrocytes

In seven control GLT1/GFP astrocytic laminae, we calculated the percentage of the ONH that was occupied by astrocyte cell bodies and processes as indicated by GFP fluorescence in 2D images taken from the middle of the zone of contact between the inner PPS and the lamina. The mean astrocyte coverage was $21\% \pm 13\%$ of the ONH area (see Supplementary Table S9 for individual astrocyte volume fraction of each control GLT1/GFP).

DVC Error Analysis

Baseline errors were calculated for the TPF images by comparing duplicate Z-stacks. In addition, the global and regional absolute average errors for each control GLT1/GFP were recorded (Supplementary Tables S10-S11). Of these

seven control eyes from six GLT1/GFP mice, four were female and three were male. These seven control eyes had low baseline errors and were analyzed for strain. The average displacement errors for the seven control eyes were $0.472 \pm 0.496 \mu\text{m}$ (1 pixel) in the nasal-temporal (X) direction, $0.227 \pm 0.218 \mu\text{m}$ (one-half pixel) in the inferior-superior (Y) direction, and $0.320 \pm 0.328 \mu\text{m}$ (one-third pixel) in the anterior-posterior (Z) direction.

The baseline errors were also calculated for the TPF duplicate Z-stacks from six eyes with chronic IOP elevation (five of these six mice had unilateral bead injections, one of the mice had bilateral bead injections). Of the six eyes with chronic IOP elevation, half were from males and half from females. One eye with chronic IOP elevation had abnormally large baseline correlation errors (see Supplementary Tables S12-S13 for global and regional baseline errors of GLT1/GFP with chronic IOP elevation, respectively) and was excluded from the strain analysis.

The mean percentage of the astrocytic lamina in control GLT1/GFP mouse explants in which DVC correlation was defined as accurate comprised $80\% \pm 10\%$ of the total ONH area, with a range of 64% to 94% (see Supplementary Table S14 for total percent correlation for each control GLT1/GFP). With the optic nerve area divided into its central 50% and its peripheral 50%, the DVC correlation was accurate in 96% of the central half, but in only 64% of the peripheral half (see Supplementary Table S15 for regional percent correlation for each control GLT1/GFP).

For explants from eyes that had undergone chronic IOP elevation, the mean percentage of the overall ONH with accurate DVC correlation was $91\% \pm 7\%$, with a range of 80% to 100% (see Supplementary Table S16 for total percent correlation for each GLT1/GFP with chronic IOP elevation). Similar to the control ONHs, accurate correlation was found in 100% of the central half of the ONH and in 83% of the peripheral ONH area (see Supplementary Table S17 for regional percent correlation for each GLT1/GFP with chronic IOP elevation).

Deformation of the Normal Astrocytic Lamina

For quantitative strain estimation in the normal astrocytic lamina, explants were imaged as Z-stacks with the confocal microscope at 10 mm Hg and 30 mm Hg, and DVC was used to calculate displacements between these two pressures. Strains

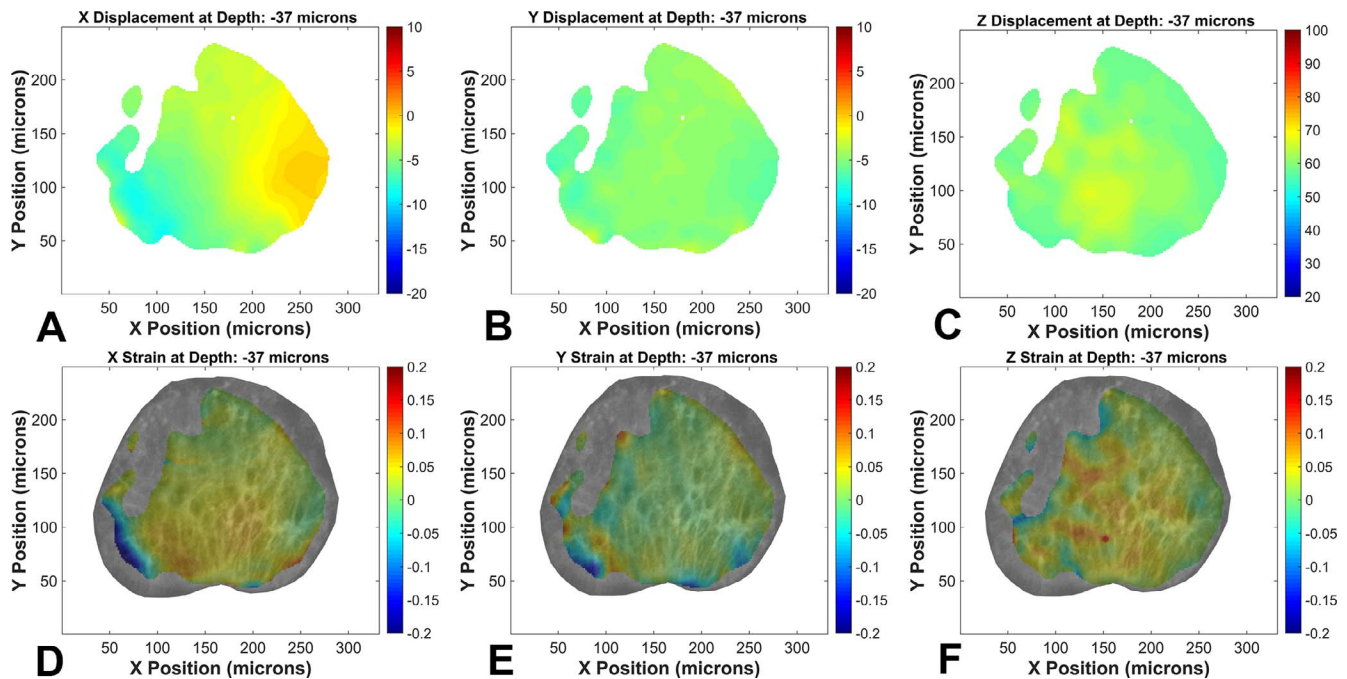


FIGURE 5. Digital volume correlation calculated displacements and strains of one control GLT1/GFP ONH astrocytic lamina (mouse 2; superior at top of images) between 10 and 30 mm Hg illustrating the (A) nasal-temporal (N-T) displacement field, (B) inferior-superior (I-S) displacement field, (C) anterior-posterior (A-P) displacement field, (D) normal strains along N-T, (E) normal strains along I-S, (F) normal strains along A-P. The color bar for the displacement plots (A, B, C) is in microns.

were calculated from fitted displacement gradients as described in Methods; an example of the displacement and strain fields for a control specimen is shown in Figure 5 (see Supplementary Figs. S18–S24 for DVC displacement and strain plots for each control GLT1/GFP). The mean Z displacement during the 2 minutes prior to imaging was $83 \pm 47 \mu\text{m}$ ($n = 7$ eyes; see Supplementary Table S25 for individual Z displacements for each control GLT1/GFP). The mean global strain in the nasal-temporal direction (E_{XX}) and the inferior-superior direction (E_{YY}) were significantly greater than zero, whereas the anterior-posterior (E_{ZZ}) direction was essentially zero and was significantly smaller than strains in the other two directions (Table 1; see Supplementary Table S26 for individual global strains for each control mouse).

We also calculated the strains for the central two-thirds of the ON area (Table 2; see Supplementary Table S27 for strain components in this region for each control GLT1/GFP). The mean nasal-temporal strain was significantly greater than zero

and significantly greater than both of the strains in the superior-inferior and anterior-posterior directions.

We also compared strains in the inner (central) half of the lamina to its outer half (peripheral). Centrally, the nasal-temporal direction was significantly greater than zero and significantly greater than either the inferior-superior or anterior-posterior directions (Table 3). The peripheral strain in the inferior-superior direction was greater than zero and greater than the anterior-posterior strain (Table 3; see Supplementary Table S28, Supplementary Figure S29 for regional strain values and DVC regions for each individual control, respectively).

ONH Perimeter

The perimeter of the astrocytic lamina was compared between 10 and 30 mm Hg for the seven eyes with TPF image sets that underwent DVC analysis (see Supplementary Table S30 for individual perimeter measurements for control GLT1/GFP). We

TABLE 1. DVC Estimated Global Strains for Astrocytic Lamina, Control and Chronic IOP Elevated

Direction	Regression Parameter		Global Strain		Adjusted P Value Comparing Directions*
	Estimate (95% CI)	P Value	Least Squares Mean (95% CI)	P Value	
Control					
NT	0.0482 (0.0257, 0.0706)	0.002	0.0521 (0.0304, 0.0739)	0.0002	<u>NT, IS</u> 0.36
IS	0.0334 (0.0110, 0.0559)		0.0374 (0.0157, 0.0592)	0.003	NT, <u>AP</u> 0.002
AP	0		0.0040 (−0.0178, 0.0258)	0.70	IS, <u>AP</u> 0.02
Chronic IOP Elevated					
NT	0.0175 (−0.0003, 0.0354)	0.04	0.0165 (0.0014, 0.0316)	0.04	<u>NT, IS</u> 0.69
IS	0.0241 (0.0063, 0.0419)		0.0231 (0.0080, 0.0382)	0.01	<u>NT, AP</u> 0.12
AP	0		−0.0010 (−0.0161, 0.0141)	0.88	IS, <u>AP</u> 0.03

* Tukey-Kramer adjustment for multiple comparisons; categories sharing an underline are not significantly different at the 0.05 level. AP, anterior-posterior; CI, confidence interval; IS, inferior-superior; NT, nasal-temporal.

TABLE 2. DVC Estimated Strains for the Central Two-Thirds of the Astrocytic Lamina, Control and Chronic IOP Elevated

Direction	Regression Parameter		Central Two-Thirds Strain		Adjusted <i>P</i> Value Comparing Directions*	
	Estimate (95% CI)	<i>P</i> Value	Least Squares Mean (95% CI)	<i>P</i> Value		
Control						
NT	0.0519 (0.0281, 0.0758)	0.0005	0.0593 (0.0423, 0.0763)	<0.0001	NT, IS	0.001
IS	−0.0014 (−0.0252, 0.0224)		0.0060 (−0.0110, 0.0230)	0.46	NT, AP	0.001
AP	0		0.0074 (−0.0096, 0.0244)	0.36	<u>IS, AP</u>	0.99
Chronic IOP Elevated						
NT	0.0284 (0.0087, 0.0480)	0.03	0.0265 (0.0092, 0.0438)	0.01	<u>NT, IS</u>	0.59
IS	0.0198 (0.0002, 0.0394)		0.0180 (0.0006, 0.0353)	0.04	NT, AP	0.02
AP	0		−0.0018 (−0.0192, 0.0155)	0.81	<u>IS, AP</u>	0.11

* Tukey-Kramer adjustment for multiple comparisons; categories sharing an underline are not significantly different at the 0.05 level. AP, anterior-posterior; CI, confidence interval; IS, inferior-superior; NT, nasal-temporal.

assessed the perimeter elongation and because the ONH shape was elliptical, we could also assess the maximum diameter, the minimum diameter, and the area of the ellipse. First, we compared the mean diameter changes from 10 to 30 mm Hg at 10 depths of the Z stack. The mean change in maximum diameter (Fig. 6) and the minimum diameter of the ONH perimeter did not differ significantly among these sampled locations in either nasal-temporal or inferior-superior directions. Thus, for the next step in the analysis it was reasonable to use the perimeter measured from the 2D Z-averaged intensity projection of each eye at 10 and 30 mm Hg, which essentially averages the perimeter measurements throughout the sampled region.

With inflation from 10 to 30 mm Hg, the control mean ONH area (calculated from the perimeter value) increased $2.4\% \pm 1.6\%$, and the mean perimeter elongation was 0.019 ± 0.016 . Both the area increase and perimeter elongation were significantly different from zero ($P = 0.016$ and 0.02 , respectively, Wilcoxon ranked sign and *t*-test, respectively). The PPS perimeter in the nasal-temporal direction had an increase in maximum diameter of $3.6\% \pm 1.9\%$, whereas the diameter in the inferior-superior direction actually became smaller by $-1.2\% \pm 1.8\%$ (difference between two directions, $P = 0.006$, *t*-test).

PPS Scleral Strain

In addition to the PPS perimeter elongation, we estimated PPS strain from the SHG images. This calculation was complicated because the anatomy of the sclera nearest to the ONH is not uniform. As detailed in a past publication,³⁵ within 500 μm of the optic nerve canal, the PPS divides into a portion that joins the ONH directly (which we have called the inner PPS) and an outer section that joins the pia mater that surrounds the optic

nerve behind the globe. This division of the sclera into sections is more dramatic than in monkey or human eyes; in the mouse, the inner and outer PPS are similar in thickness, whereas in the monkey or human eye much more of the PPS remains to join the ONH as its inner portion. Furthermore, the blood vessels that enter the mouse eye occupy three large channels on the inferior side of the optic nerve, passing through the sclera directly and into the ONH (Fig. 1D). The vessels leave their scleral channels and enter the inferior optic nerve just behind the eye, resulting in a kidney-bean shape to the astrocytic lamina and a fibrovascular indentation in its inferior zone.

The zone of the inner sclera that directly connects to the astrocytic lamina is typically less than 100 μm in length anterior-posteriorly. In attempting to image this zone uniformly around the astrocytic lamina, it is difficult to include the same level all across an image plane because of the tilting of the ONH as it passes through the canal. As a result of these anatomic features, we obtained DVC correlations in the PPS in regions of every eye, but it was uncommon to obtain images containing comparable portions of inner PPS throughout the complete perimeter (Fig. 7).

An example of the DVC-calculated displacement and strain measurements from SHG images is presented in Figure 8. As described, the PPS junctional zone to the ONH provided usable data for approximately three-fourths of the inner PPS. In the portions of the PPS for which analysis was possible, the displacements averaged approximately 10 μm , and the strains were 1% to 2%.

Effect of Chronic IOP Elevation on Astrocyte Structure, Laminal Strain, and ONH Perimeter

Two-photon fluorescence images of explants from mice that had undergone 1 to 3 days of chronic IOP elevation using the

TABLE 3. Central Versus Peripheral Lamina Strains

Direction	Regression Parameter		Strain		Adjusted <i>P</i> Value Comparing Directions*	
	Estimate (95% CI)	<i>P</i> Value	Least Squares Mean (95% CI)	<i>P</i> Value		
Central						
NT	0.0529 (0.0134, 0.0925)	0.01	0.0607 (0.0348, 0.0867)	0.0003	NT, IS	0.01
IS	−0.0135 (−0.0530, 0.0261)		−0.0057 (−0.0317, 0.0203)	0.64	NT, AP	0.03
AP	0		0.0078 (−0.0182, 0.0338)	0.53	<u>IS, AP</u>	0.74
Peripheral						
NT	0.0293 (−0.0490, 0.1075)	0.03	0.0371 (−0.0297, 0.1040)	0.25	<u>NT, IS</u>	0.13
IS	0.1056 (0.0273, 0.1838)		0.1134 (0.0466, 0.1803)	0.003	<u>NT, AP</u>	0.70
AP	0		0.0079 (−0.0590, 0.0747)	0.80	IS, AP	0.03

* Tukey-Kramer adjustment for multiple comparisons; categories sharing an underline are not significantly different at the 0.05 level. AP, anterior-posterior; CI, confidence interval; IS, inferior-superior; NT, nasal-temporal.

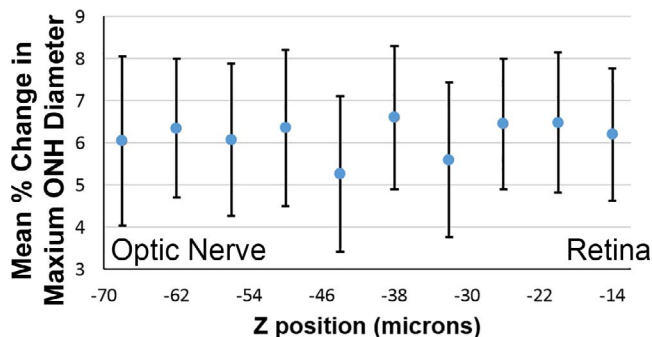


FIGURE 6. Mean percent change in the maximum ONH diameter (N:T) of control GLT1/GFP at each of 10 locations, equally spaced in the Z-stack from nearer to the retina (*right*) to the posterior astrocytic lamina (*left*), for IOP change between 10 and 30 mm Hg. The parameter here was the maximum diameter of the perimeter of the ONH analyzed as an ellipse.

bead injection glaucoma model were compared with those of fellow control eyes without chronic IOP elevation. There were alterations in the position and shape of ONH astrocytes after chronic IOP elevation. Specifically, control astrocytic processes were in the plane of the image, running from one side of the ONH perimeter to the other. In IOP elevation explants, many astrocyte processes were seen as oblique or round profiles, indicating that they were more oriented with the long axis of the ONH. To ensure that this finding was not simply an alteration in the specific expression of the fluorescent marker in the GLT1/GFP mice, we performed comparisons of IOP elevation and control ONH astrocytes in GFAP-labeled, histological sections of the same explants. Both GFP and GFAP labels showed the same apparent reorientation of processes

from side to side in controls toward a more longitudinal pattern in the IOP elevation specimens (Fig. 8).

The strain in the astrocytic lamina was estimated from five of the six eyes with chronic IOP elevation of 1 to 3 days prior to TPF imaging of their explants (see Supplementary Figs. S31–S36 for DVC displacement and strain plots for each GLT1/GFP with chronic IOP elevation). The mean Z displacement during the 1 minute prior to imaging was $92 \pm 64 \mu\text{m}$ ($n = 5$ eyes; see Supplementary Table S37 for individual Z displacements for each GLT1/GFP with chronic IOP elevation). Both the mean global ONH strain and the mean strain within the central two-thirds of the ON area were significantly smaller than the control value in the nasal-temporal direction ($P = 0.007$ and $P = 0.028$ respectively, *t*-test, Table 1; see Supplementary Tables S38–S40 and Figure S41 for individual global strains, strains within two-thirds of the ON area, regional strains, and DVC regions for GLT1/GFP with chronic IOP elevation, respectively). The mean regional peripheral nasal-temporal strains for eyes with chronic IOP elevation were also significantly smaller than for controls ($P = 0.042$, *t*-test).

In the glaucoma eyes, the mean global strains in the nasal-temporal and the inferior-superior direction were similar to each other and were both greater than in the anterior-posterior direction, which was nearly zero (Table 1; see Supplementary Table S38 for global strains for each individual eye with chronic IOP elevation). The findings were comparable when only the central two-thirds of the lamina was included (Table 2).

To estimate PPS strain in the experimental glaucoma eye explants, we compared their ONH area change and perimeter elongation to that of controls (see Supplementary Table S42 for individual PPS opening perimeter measurements for GLT1/GFP with chronic IOP elevation). After 1 to 3 days of IOP elevation, explants from six eyes that were imaged with TPF at the baseline IOP of 10 mm Hg had ONH perimeters that were a mean of 7.5% larger than controls. Mean ONH area was 17.1% larger than controls ($P = 0.035$, Mann-Whitney *U* test). When

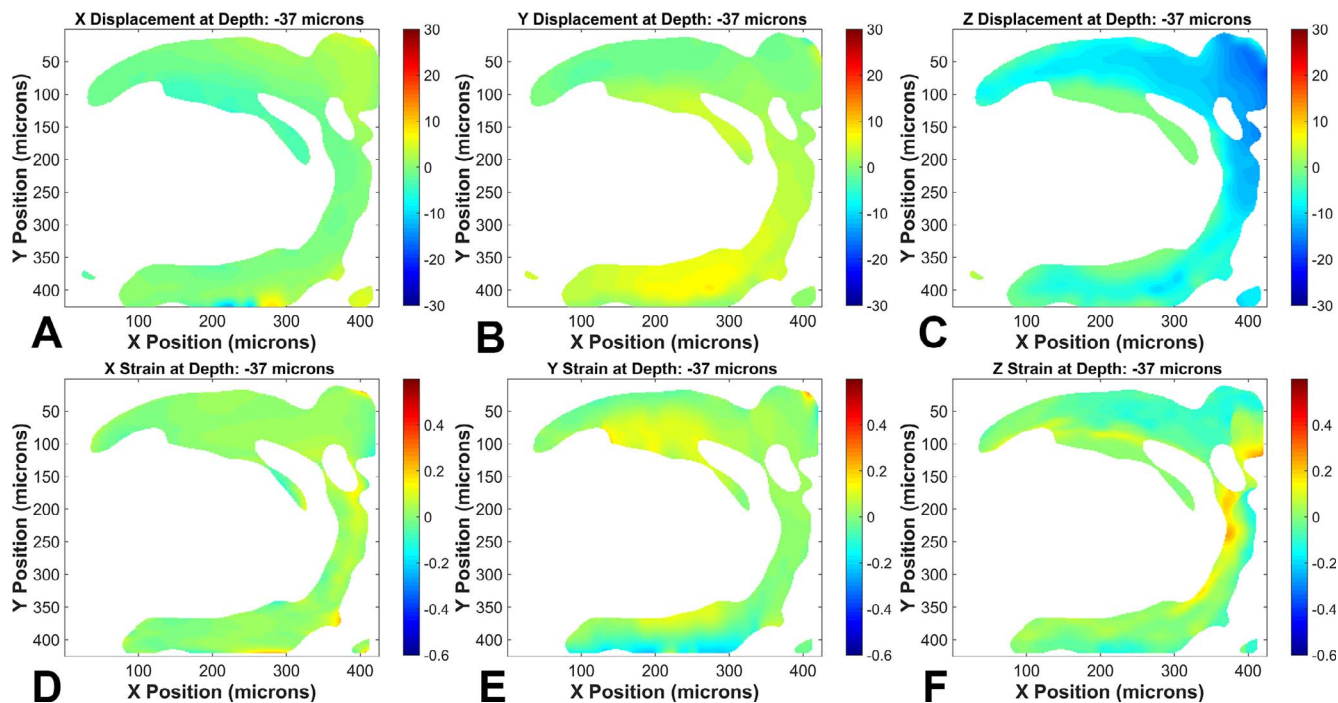


FIGURE 7. Example from one control GLT1/GFP ONH of displacements (A, B, C) and strains (D, E, F) in the X, Y, and Z directions (A, D: X = nasal-temporal direction; B, E: Y = inferior-superior direction; and C, F: Z = anterior-posterior direction) between 10 and 20 mm Hg. The superior ONH (at the *top* of the images) successfully correlated, along with the inferior and nasal portions of the PPS. The temporal portion of the PPS did not correlate (at *left* of each image). The *color bar* for the displacement plots (A, B, C) is in microns.

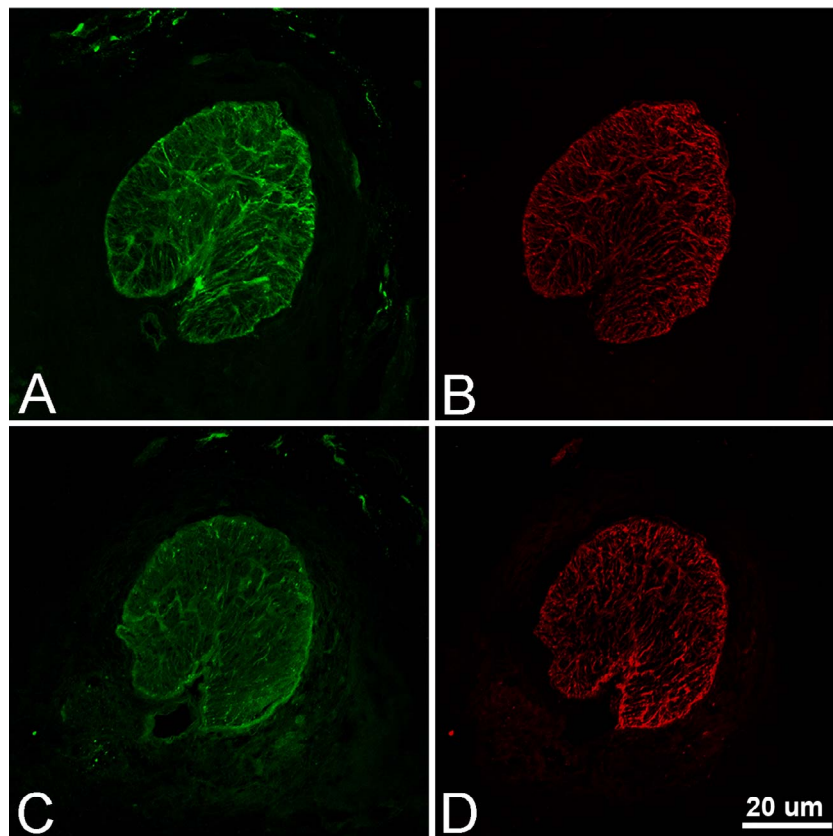


FIGURE 8. Confocal images of control (A, B) and chronic IOP elevation (C, D) in cryosections of ONH (GFP, green; GFAP, red; 20 \times). Although astrocyte structure appears generally in the plane of section in control, the change in orientation in chronic IOP elevation eye leads to oblique sections through many astrocytes.

the chronic IOP elevation eye explants were inflated from 10 to 30 mm Hg, the perimeter elongation was 0.012 ± 0.012 , or 37% less than that of controls and the mean ONH area increased only $0.9\% \pm 0.4\%$, whereas the control mean increase was $2.4\% \pm 1.6\%$ ($P = 0.0012$, Mann-Whitney U test).

DISCUSSION

We developed methods to investigate the mechanical response of the mouse ONH and PPS to acute and chronic changes in IOP. There has been extensive use of mice in both spontaneous genetic models of glaucoma³⁶ and chronic, artificially elevated IOP models³⁷ to elucidate pathogenic mechanisms of glaucoma. Previous studies of mouse,²⁵ monkey,³⁸ and human¹² glaucoma eyes show altered mechanical responses in the posterior sclera, but the behavior of the ONH itself was not included because it is technically more challenging. Our explant model provides an opportunity to provide detailed analysis of the mouse ONH. It shows stability in both the cellular structure in the astrocytic lamina and for inflation testing over periods of 3 hours. The resulting strain measurements in the astrocytic lamina from TPF imaging and DVC correlation cover an average of 80% of the tissue within the ONH for controls. The IOP range used here includes both physiological and elevated IOP levels sufficient to cause RGC death in chronic models; hence, the strains measured are relevant to those known to lead to initial axonal injury. We found that the astrocytic lamina deformed under pressure with strain magnitudes of 1% to 6% strain, which are in a similar range to those measured for the human lamina cribrosa.^{10,26,39} The present model can detail the behavior of the whole

astrocytic lamina as a 3D unit compared to histological methods. Because we can image both the sclera and the astrocytic lamina in the same eye in one experimental session, the model can assess the strain behavior of the two structures as a unit.

There were differences in both structure and behavior in the explants after 1 to 3 days of IOP elevation. Chronic IOP elevation explants had strains that were stiffer than controls, especially nasal-temporally. Further study of different durations of chronic IOP elevations will be valuable to provide details of this change. The PPS perimeter and the ONH area were larger after only 1 to 3 days of IOP increase. We have previously documented that the axial length of the mouse eye enlarges with the chronic glaucoma model.¹⁹ Not only was the ONH larger but also its response to inflation from 10 to 30 mm Hg (perimeter elongation) was decreased by nearly threefold. Clearly, there are relatively rapid shifts in posterior ocular tissues caused by IOP elevation that can be studied in this model.

In control explants, nasal-temporal strains were greater in the central ONH versus the ONH periphery. Similar studies of human lamina strains by our group found greater shear strains in the peripheral lamina than centrally.¹⁴ However, when portions of the astrocytic lamina could not be included as useful data, it was more common that the unusable area was peripherally in the ONH. The sampling of information may play a role in how accurately such methods portray the true regional behavior. We have not yet studied enough specimens to determine if sex or age affect these measurements, and these features will be studied in future experiments.

The shape of the canal through the mouse PPS is horizontally oval, and this may contribute to the difference in

regional strains. Furthermore, the group of large blood vessels just outside the ONH inferiorly may provide an asymmetric effect on ONH strain. Consistent with these features, the change in the diameter of the ONH canal under inflation in the normal mouse eye was significantly larger in the nasal-temporal direction than in the inferior-superior direction, where it actually became narrower.

Our initial measurements of the volume fraction of astrocytes and their detailed structural changes with IOP level provide a baseline for studies that investigate chemical and therapeutic approaches to this tissue's role in glaucoma. Astrocytes are mechanosensitive,⁴⁰ and their response to IOP change can assist the study of pathways by which RGC injury occurs. Previous studies of mice with selectively fluorescent astrocytes show dramatic and reversible changes at 3 days after acute IOP elevation.⁴¹ Optic nerve head astrocytes in mice have long processes that can span the ONH,¹⁷ and astrocytes showed significant morphological changes after 3 days of IOP elevation, though the previously reported changes were less severe in experimental glaucoma than after nerve crush. These included cell body and primary process hypertrophy and loss of branches, leading to a decrease in the volume fraction occupied by the cell processes.⁴² We have demonstrated that astrocytic changes begin to occur in just 2 hours. With chronic IOP elevation for 3 days, astrocyte processes reorient to a more anterior-posterior direction, as seen histologically in rat glaucoma.⁴³ Fibroblasts and other cells orient to the direction of stress,^{44,45} and our data suggest that this may be true of ONH astrocytes. Cultured mouse astrocytes respond to stretch by releasing adenosine triphosphate (ATP).⁴⁶ Transmission electron microscopic study suggests that ONH astrocytes retract processes in contact with PPS after acute IOP elevation.⁴⁷ Astrocytes are normally interconnected by connexin-based gap junctions in a syncytium, and these may be altered by mechanical stress.⁴⁸ Our explant model permits real-time examination of the acute events in the astrocytic response to IOP.

There was resistance in the past to the use of rodents in glaucoma research because of the fact that the mouse (and rat) ONH consists of astrocytes and lacks connective tissue as is present in the human lamina cribrosa. Yet, the mouse eye exhibits a fundamental feature of glaucoma, namely injury to RGC axons at the ONH when IOP is chronically increased, with selective death of RGCs and the preservation of other retinal neurons. Jakobs and colleagues²⁰ first reported that the mouse lamina astrocytes are configured similarly to the astrocyte-lined collagen beams in human ONH. Furthermore, the mouse PPS has the same concentric configuration of collagen and elastin as human PPS. Studies of scleral alteration in mouse glaucoma demonstrate axial scleral elongation, increase in stiffness, loss of nonfibrillar matrix, thickening and reorientation of collagenous fiber layers,³² decreased scleral permeability,⁴⁹ increased scleral fibroblast activity and division, and increased integrin-linked and actin-cytoskeletal signaling by proteomic analysis.⁵⁰

Our strain measurements were taken 1 minute after altering IOP because there was substantial axial length increase and, hence, rapid astrocytic lamina movement was induced. A qualitatively similar movement of the lamina was observed in experimental monkey glaucoma,⁵¹ and the volume expansion of the human eye with an increase in pressure has been well studied.⁵² Our measurements more appropriately focus on the alterations within the ONH after the overall global movement.

The explant model has potential limitations that must be considered. The blood supply of the animal is absent, and this may influence cellular behavior over extended periods of observation. The removal of the optic nerve behind the eye, although necessary to obtain detailed imaging, could induce an

injury effect on the astrocytic lamina. There is a small hydrostatic/osmotic pressure within the intact optic nerve—related to cerebrospinal fluid pressure, which is not present in our model testing. Because this is typically 3 to 5 mm Hg, its absence increases the translaminar pressure differential by a small amount in our tests. The method uses the natural contrast patterns provided in TPF images (for the astrocytic lamina) and SHG imaging (for the collagen structure in the PPS), thus the DVC accuracy and uncertainty varies with the SHG and TPF image quality and the contrast provided by the imaged collagen and astrocytic beam structures. The peripheral astrocytic lamina had poorer correlation than the more central lamina, as shown by our comparisons of strain for the whole lamina, for its central two-thirds and the central one-half. Digital volume correlation is unable to correlate large, overly dark, or overly bright areas. The complex structure of the mouse PPS, in particular, presents challenges for the correlation of its complete perimeter because of natural variations in signal quality, such as the presence of blood vessel insertion sites, which appear as dark spots, and the scleral curvature. Spacing between Z-slices is larger (1 μm) than the pixel size in the X-Y plane (0.415 μm). As a result, there is an inherent resolution difference in strain estimation between the Z direction and X-Y. Whether this causes the nearly undetectable strain in Z in our lamina measurements awaits further design improvements.

Although we were able to estimate PPS behavior with perimeter elongation measurements, our method for strain estimation by SHG did not produce useful data in some specimens. To solve this practical problem, we developed an improved imaging method for imaging the PPS that combines the signal from collagen in SHG and from elastin in TPF. This has shown promise in human PPS tissue and in initial mouse specimens. We also plan to develop an inverse finite element model to analyze the relationship between the stresses, strains, and mechanical properties of the combined PPS and ONH system.

Pharmacological alterations in the response of the PPS and ONH tissues represent a new glaucoma treatment area, scleral neuroprotection.⁵³ Human glaucoma eyes show higher transforming growth factor β gene expression and protein levels in trabecular meshwork⁵⁴ and ONH.⁵⁵⁻⁵⁷ Losartan suppresses transforming growth factor β signaling and decreased RGC loss in experimental mouse glaucoma.¹⁹ The explant model can provide a means to assess potential pharmacological modifications of the PPS-ONH that confer resistance to glaucoma damage.

In summary, we have implemented a whole-eye explant model in which real-time evaluation of intracellular processes and biomechanical measurements of the ONH can be made by altering IOP under SHG and TPF imaging. In genetically modified mice with fluorescently tagged components, the initial mechanical events produced by IOP elevation can be studied in detail. Initial data on chronic IOP elevations of 1 to 3 days identified reconfiguration of ONH astrocytes, enlargement of the ONH perimeter, and stiffening of the astrocytic lamina and PPS opening.

Acknowledgments

Supported in part by Public Health Service (PHS) Grants EY 02120 and EY 01765 (HAQ and Wilmer Institute Core grant), EY021500 National Science Foundation (NSF) Career Award CMMI-1253453, Brightfocus Foundation Grant G2015132 (TDN), and by unrestricted support from Saranne and Livingston Kosberg and William T. Forrester. The authors alone are responsible for the content and writing of the paper.

Disclosure: C. Nguyen, None; D. Midgett, None; E.C. Kimball, None; M.R. Steinhart, None; T.D. Nguyen, None; M.E. Pease, None; E.N. Oglesby, None; J.L. Jefferys, None; H.A. Quigley, None

References

- Bengtsson B, Heijl A. Diurnal IOP fluctuation: not an independent risk factor for glaucomatous visual field loss in high-risk ocular hypertension. *Graefes Arch Clin Exper Ophthalmol*. 2005;243:513-518.
- Nouri-Mahdavi K, Hoffman D, Coleman A. Predictive factors for glaucomatous visual field progression in the Advanced Glaucoma Intervention Study. *Ophthalmology*. 2004;111:1627-1635.
- De Moraes CG, Juthani VJ, Liebmann JM. Risk factors for visual field progression in treated glaucoma. *Arch Ophthalmol*. 2011;129:562-568.
- Burgoyne CF, Downs JC, Bellezza AJ, Suh JK, Hart RT. The optic nerve head as a biomechanical structure: a new paradigm for understanding the role of IOP-related stress and strain in the pathophysiology of glaucomatous optic nerve head damage. *Prog Retin Eye Res*. 2005;24:39-73.
- Ethier CR. Scleral biomechanics and glaucoma—a connection? *Can J Ophthalmol*. 2006;41:9-11.
- Coudrillier B, Boote C, Quigley HA, Nguyen TD. Scleral anisotropy and its effects on the mechanical response of the optic nerve head. *Biomech Model Mechanobiol*. 2013;12:941-963.
- Sigal IA, Yang H, Roberts MD, et al. IOP-induced lamina cribrosa deformation and scleral canal expansion: independent or related? *Invest Ophthalmol Vis Sci*. 2011;52:9023-9032.
- Sigal IA, Flanagan JG, Ethier CR. Factors influencing optic nerve head biomechanics. *Invest Ophthalmol Vis Sci*. 2005;46:4189-4199.
- Quigley HA, Nickells RW, Kerrigan LA, Pease ME, Thibault DJ, Zack DJ. Retinal ganglion cell death in experimental glaucoma and after axotomy occurs by apoptosis. *Invest Ophthalmol Vis Sci*. 1995;36:774-786.
- Kerrigan LA, Zack DJ, Quigley HA, Smith SD, Pease ME. TUNEL-positive ganglion cells in human primary open angle glaucoma. *Arch Ophthalmol*. 1997;115:1031-1035.
- Quigley HA, Addicks EM. Regional differences in the structure of the lamina cribrosa and their relation to glaucomatous optic nerve damage. *Arch Ophthalmol*. 1981;99:137-143.
- Dandona L, Quigley HA, Brown AE, Enger C. Quantitative regional structure of the normal human lamina cribrosa. A racial comparison. *Arch Ophthalmol*. 1990;108:393-398.
- Quigley HA, Addicks EM, Green WR. Optic nerve damage in human glaucoma. III. Quantitative correlation of nerve fiber loss and visual field defect in glaucoma, ischemic neuropathy, disc edema, and toxic neuropathy. *Arch Ophthalmol*. 1982;100:135-146.
- Midgett DE, Pease ME, Jefferys JL, et al. The pressure-induced deformation response of the human lamina cribrosa: analysis of regional variations [published online ahead of print January 17, 2017]. *Acta Biomaterialia*. doi:10.1016/j.actbio.2016.12.054.
- Quigley HA, Broman A. The number of persons with glaucoma worldwide in 2010 and 2020. *Br J Ophthalmol*. 2006;90:151-156.
- Coudrillier B, Pijanka JK, Jefferys JL, et al. Glaucoma-related changes in the mechanical properties and collagen micro-architecture of the human sclera. *PLoS One*. 2015;10:e0131396.
- Girard MJA, Suh J-KF, Mottlang M, Burgoyne CF, Downs JC. Biomechanical changes in the sclera of monkey eyes exposed to chronic IOP elevations. *Invest Ophthalmol Vis Sci*. 2011;52:5656-5669.
- Myers KM, Cone FE, Quigley HA, Gelman SE, Pease ME, Nguyen TD. The in vitro inflation response of mouse sclera. *Exp Eye Res*. 2010;91:866-875.
- Quigley HA, Pitha IF, Welsbie DS, et al. Losartan treatment protects retinal ganglion cells and alters scleral remodeling in experimental glaucoma. *PLoS One*. 2015;10:e0141137.
- Sun D, Lye-Barthel M, Masland RH, Jakobs TC. The morphology and spatial arrangement of astrocytes in the optic nerve head of the mouse. *J Comp Neurol*. 2009;516:1-19.
- Morrison JC, Cepurna WO, Guo Y, Johnson EC. Pathophysiology of human glaucomatous optic nerve damage: insights from rodent models of glaucoma. *Exp Eye Res*. 2011;93:156-164.
- Cone FE, Steinhart MR, Oglesby EN, Kalesnykas G, Pease ME, Quigley HA. The effects of anesthesia, mouse strain and age on intraocular pressure and an improved murine model of experimental glaucoma. *Exp Eye Res*. 2012;99:27-35.
- Fernandes KA, Harder JM, Williams PA, et al. Using genetic mouse models to gain insight into glaucoma: past results and future possibilities. *Exp Eye Res*. 2015;141:42-56.
- Pijanka JK, Coudrillier B, Ziegler K, et al. Quantitative mapping of collagen fiber orientation in non-glaucoma and glaucoma posterior human sclerae. *Invest Ophthalmol Vis Sci*. 2012;53:5258-5270.
- Pijanka JK, Cone-Kimball E, Pease ME, et al. Changes in scleral collagen organization associated with murine chronic experimental glaucoma. *Invest Ophthalmol Vis Sci*. 2014;55:6554-6564.
- Kendall KR, Quigley HA, Kerrigan LA, Pease ME, Quigley EN. Primary open-angle glaucoma is not associated with photoreceptor loss. *Invest Ophthalmol Vis Sci*. 1995;36:200-205.
- Howell GR, Libby RT, Jakobs TC, et al. Axons of retinal ganglion cells are insulted in the optic nerve early in DBA/2J glaucoma. *J Cell Biol*. 2007;179:1523-1537.
- Nguyen C, Cone FE, Nguyen TD, et al. Studies of scleral biomechanical behavior related to susceptibility for retinal ganglion cell loss in experimental mouse glaucoma. *Invest Ophthalmol Vis Sci*. 2013;54:1767-1780.
- Girard MJ, Beotra MR, Chin KS, et al. In vivo 3-dimensional strain mapping of the optic nerve head following intraocular pressure lowering by trabeculectomy. *Ophthalmology*. 2016;123:1190-1200.
- Coudrillier B, Campbell IC, Read AT, et al. Effects of peripapillary scleral stiffening on the deformation of the lamina cribrosa. *Invest Ophthalmol Vis Sci*. 2016;57:2666-2677.
- Regan MR, Huang YH, Kim YS, et al. Variations in promoter activity reveal a differential expression and physiology of glutamate transporters by glia in the developing and mature CNS. *J Neurosci*. 2007;27:6607-6619.
- Zhuo L, Sun B, Zhang C-L, Fine A, Chiu S-Y, Messing A. Live astrocytes visualized by green fluorescent protein in transgenic mice. *Devel Biol*. 1997;187:36-42.
- Schindelin J, Arganda-Carreras I, Frise E, et al. Fiji: an open-source platform for biological-image analysis. *Nat Methods*. 2012;9:676-682.
- Bar-Kochba E, Toyjanova J, Andrews E, Kim K, Franck C. A fast iterative digital volume correlation algorithm for large deformations. *Exp Mech*. 2015;55:261-274.
- Cone-Kimball E, Nguyen C, Oglesby EN, Pease ME, Steinhart MR, Quigley HA. Scleral structural alterations associated with chronic experimental intraocular pressure elevation in mice. *Mol Vis*. 2013;19:2023-2039.
- John SW, Smith RS, Savinova OV, et al. Essential iris atrophy, pigment dispersion, and glaucoma in DBA/2J mice. *Invest Ophthalmol Vis Sci*. 1998;39:951-962.

37. Cone FE, Gelman SE, Son JL, Pease ME, Quigley HA. Differential susceptibility to experimental glaucoma among 3 mouse strains using bead and viscoelastic injection. *Exp Eye Res.* 2010;91:415-424.
38. Downs JC, Suh JKF, Thomas KA, et al. Viscoelastic material properties of the peripapillary sclera in normal and early-glaucoma monkey eyes. *Invest Ophthalmol Vis Sci.* 2005;46:540-546.
39. Sigal IA, Grimm JL, Jan NJ, Reid K, Minckler DS, Brown DJ. Eye-specific IOP-induced displacements and deformations of human lamina cribrosa. *Invest Ophthalmol Vis Sci.* 2014;55:1-15.
40. Choi HJ, Sun D, Jakobs TC. Astrocytes in the optic nerve head express putative mechanosensitive channels. *Mol Vis.* 2015;21:749-766.
41. Sun D, Qu J, Jakobs TC. Reversible reactivity by optic nerve astrocytes. *Glia.* 2013;61:1218-1235.
42. Lye-Barthel M, Sun D, Jakobs TC. Morphology of astrocytes in a glaucomatous optic nerve. *Invest Ophthalmol Vis Sci.* 2013;54:909-917.
43. Tehrani S, Johnson EC, Cepurna WO, Morrison JC. Astrocyte processes label for filamentous actin and reorient early within the optic nerve head in a rat glaucoma model. *Invest Ophthalmol Vis Sci.* 2014;55:6945-6952.
44. Faust U, Hampe N, Rubner W, et al. Cyclic stress at mHz frequencies aligns fibroblasts in direction of zero strain. *PLoS One.* 2011;6:e28963.
45. Prager-Khoutorsky M, Lichtenstein A, Krishnan R, et al. Fibroblast polarization is a matrix-rigidity-dependent process controlled by focal adhesion mechanosensing. *Nature Cell Biol.* 2011;13:1457-1465.
46. Beckel JM, Argall AJ, Lim JC, et al. Mechanosensitive release of adenosine 5'-triphosphate through pannexin channels and mechanosensitive upregulation of pannexin channels in optic nerve head astrocytes: a mechanism for purinergic involvement in chronic strain. *Glia.* 2014;62:1486-1501.
47. Dai C, Khaw PT, Yin ZQ, Li D, Raisman G, Li Y. Structural basis of glaucoma: The fortified astrocytes of the optic nerve head are the target of raised intraocular pressure. *Glia.* 2012;60:13-28.
48. Hernandez MR, Miao H, Lukas T. Astrocytes in glaucomatous optic neuropathy. *Prog Brain Res.* 2008;173:353-373.
49. Pease ME, Oglesby EN, Cone-Kimball E, et al. Scleral permeability varies by mouse strain and is decreased by chronic experimental glaucoma. *Invest Ophthalmol Vis Sci.* 2014;55:2564-2573.
50. Oglesby EN, Tezel G, Cone-Kimball E, et al. Scleral fibroblast response to experimental glaucoma in mice. *Mol Vis.* 2016;22:82-99.
51. Yang H, Williams G, Downs JC. Posterior (outward) migration of the lamina cribrosa and early cupping in monkey experimental glaucoma. *Invest Ophthalmol Vis Sci.* 2011;52:7109-7121.
52. Silver DM, Geyer O. Pressure-volume relation for the living human eye. *Curr Eye Res.* 2000;20:115-120.
53. Quigley HA, Cone FE. Development of diagnostic and treatment strategies for glaucoma through understanding and modification of scleral and lamina cribrosa connective tissue. *Cell Tissue Res.* 2013;353:231-244.
54. Sethi A, Mao W, Wordinger RJ, Clark AF. Transforming growth factor- β induces extracellular matrix protein cross-linking lysyl oxidase (LOX) genes in human trabecular meshwork cells. *Invest Ophthalmol Vis Sci.* 2011;52:5240-5250.
55. Johnson EC, Cepurna WO, Doser TA, Morrison JC. Global changes in optic nerve head gene expression after exposure to elevated intraocular pressure in a rat glaucoma model. *Invest Ophthalmol Vis Sci.* 2007;48:3161-3177.
56. Pena JDO, Taylor AW, Ricard CS, Vidal I, Hernandez MR. Transforming growth factor isoforms in human optic nerve heads. *Br J Ophthalmol.* 1999;83:209-218.
57. De Groef L, Van Hove I, Dekeyster E, Stalmans I, Moons L. MMPs in the neuroretina and optic nerve: modulators of glaucoma pathogenesis and repair? *Invest Ophthalmol Vis Sci.* 2014;55:1953-1964.